

Hydrocarbon chemistry in inner regions of planet forming disks

J.Kanwar^{1,2,3}, I.Kamp¹, P.Woitke², Ch.Rab^{4,5}, W.F.Thi⁴, and M.Min⁶

¹ Kapteyn Astronomical Institute, University of Groningen, P.O. Box 800, 9700 AV Groningen, The Netherlands e-mail: kanwar@astro.rug.nl

² Space Research Institute, Austrian Academy of Sciences, Schmiedlstr. 6, A-8042, Graz, Austria

³ TU Graz, Fakultät für Mathematik, Physik und Geodäsie, Petersgasse 16 8010 Graz, Austria

⁴ Max Planck Institute for Extraterrestrial Physics, Giessenbachstrasse, 85741 Garching, Germany

⁵ University Observatory, Faculty of Physics, Ludwig-Maximilians-Universität München, Scheinerstr. 1, 81679 Munich, Germany

⁶ SRON Netherlands Institute for Space Research, Niels Bohrweg 4, 2333 CA Leiden, Netherlands

Received 2023; accepted 2023

ABSTRACT

Context. The analysis of the mid-infrared spectra helps understanding the composition of the gas in the inner, dense and warm terrestrial planet forming region of disks around young stars. ALMA has detected hydrocarbons in the outer regions of the planet forming disk and Spitzer detected C_2H_2 in the inner regions. JWST- MIRI provides high spectral resolution observations of C_2H_2 and a suite of more complex hydrocarbons are now reported. Interpreting the fluxes observed in the spectra is challenging and radiation thermo-chemical codes are needed to properly take into account the disk structure, radiative transfer, chemistry and thermal balance. Various disk physical parameters like the gas-to-dust ratio, dust evolution including radial drift, dust growth and settling can affect the fluxes observed in the mid-IR. Still, thermo-chemical disk models were not always successful in matching all observed molecular emission bands simultaneously.

Aims. The goal of this project is two-fold. We analyse the warm carbon chemistry in the inner regions of the disk, i.e. within 10 au to find pathways forming C_2H_2 potentially missing from the existing chemical networks. Second, we analyse the effect of the new chemistry on the line fluxes of acetylene.

Methods. We use radiative thermo-chemical disk code PRODIMO to expand the hydrocarbon chemistry that occurs in a typical standard T Tauri disks. We used the UMIST and the KIDA rate databases for collecting reactions for the species. We include a number of three-body and thermal decomposition reactions from STAND2020 network. We included isotopomers for the species that were present in the databases. The chemistry is then analysed in the regions that produce observable features in the mid-infrared spectra. The effect of expanding the hydrocarbon chemistry on the mid-infrared spectra is studied.

Results. Acetylene is formed via two pathways in the surface layers of disks: neutral-neutral and ion-neutral. They proceed via the hydrogenation of C or C^+ , respectively. Thus, the abundances of C, C^+ , H and H_2 affect the formation of C_2H_2 . Therefore, also the formation of H_2 indirectly affects the abundance of acetylene. Chemisorbed H is more efficient in forming H_2 compared to physisorbed H at warm temperatures and hence increases the abundance of C_2H_2 .

Conclusions. We provide a new extended warm chemical network that considers up to eight carbon atom long species, takes into account different isotopomers and can form the building block of PAHs C_6H_6 . For a standard T Tauri disk with a canonical value of gas-to-dust mass, the line fluxes increase only a factor of less than 2. JWST is now detecting hydrocarbons like methane, acetylene and C_4H_2 in disks having high C/O ratio. Hence this new extended warm hydrocarbon network will aid in interpreting the observed mid-infrared fluxes.

Key words. astrochemistry – inner disk – hydrocarbons – mid-IR spectra – JWST-MIRI

1. Introduction

The inner region of a planet forming disk (~ 10 au) is warm (200–1000 K), dense (10^8 – 10^{15} cm^{-3}) and is the nursery for the terrestrial planets (Henning & Semenov 2013). Understanding the rich molecular chemistry in this region can help predict the composition of terrestrial planets. Studies of the chemistry in this region are possible with mid-infrared spectroscopy which traces the warm surface layers.

Carbon is one of the most abundant elements and is essential for life. The warm molecular layer is abundant in H_2 , carbon and shielded from UV photons by dust, H_2 (Draine & Bertoldi 1996), H_2O (Bethell & Bergin 2009; Duval et al. 2022), thus paving the way for a rich organic chemistry. Carbon based molecules like CO, CO_2 , C_2H_2 have been observed using Spitzer (e.g. Carr & Najita 2011; Salyk et al. 2008; Pontoppidan et al. 2010). Other

hydrocarbons like $c-C_3H_2$ (Qi et al. 2013), C_2H (Bergin et al. 2016) have been detected in the outer disks by the MAPS consortium (Ilee et al. 2021; Guzmán et al. 2021). With the advent of JWST, a plethora of new species are discovered due to its high sensitivity and increased spectral resolution compared to Spitzer. Among the new detections (Tabone et al. 2023, A. M. Arabhavi 2023) are various hydrocarbons emitting in the mid-infrared region as predicted by Bast et al. (2013).

There have been various studies on hydrocarbon chemistry in different environments (temperatures, pressures initial abundances, radiation etc.) like in molecular clouds, AGB stars, planetary nebulae and planet forming disks. Carbon chains can form at the early stages of cloud evolution before C gets locked in CO in warm carbon chain chemistry in molecular clouds. Experimental study by Santoro et al. (2020) investigated the gas-phase interaction of C and C_2 with C_2H_2 leading to polyacetylenic

chains and poly-cyclic aromatic hydrocarbons (PAHs) for the outer layers of C-rich AGB and protoplanetary nebulae. Benzene is shown to form in a bottom up approach in the inner 3 au of the planet forming disk and its abundance structure is affected by the uncertainty in the adsorption energies assumed for it (Woods & Willacy 2007). Kress et al. (2010) studied the formation of poly-cyclic aromatic hydrocarbons (PAHs) and calculated the position of the soot line beyond which PAHs are destroyed in disks. A comparative study on chemistry around the stars with spectral types from A to M showed different abundance structures of C_2H_2 and set of pathways leading to its formation in X-ray and UV dominated regions (Walsh et al. 2015).

Hydrocarbons have been detected in the ISM and molecular clouds with only C_2H_2 detected in disks around T Tauri stars and CH_4 , C_4H_2 , C_6H_6 detected (Tabone et al. 2023) in disks around very low mass stars in the mid-IR. There have been numerous attempts to reproduce the observational flux levels through thermo-chemical modelling. Earlier work (e.g. Woitke et al. 2018; Greenwood et al. 2019a,b; Anderson et al. 2021) proposed high gas-dust, dust evolution (including radial drift, growth, settling) and a high C/O ratio to interpret the observed fluxes of C_2H_2 and H_2O . Little work went in looking in more detail into the formation pathways of C_2H_2 which explains the need to revisit the chemical networks used widely in the disk community.

Hence, in this paper, the focus is on expanding the hydrocarbon chemistry and studying how this affects the mid-infrared spectra especially in the light of new JWST data. The radiation thermo-chemical modelling code PRODIMO (Woitke et al. 2009) is used to determine the disk structure of a typical T Tauri disk (Woitke et al. 2016). The hydrocarbon chemistry is expanded beyond the large DIANA chemistry (Kamp et al. 2017). The key ingredients of the disk modelling code PRODIMO, the large DIANA chemical network and the description of the extension of the chemical network for hydrocarbons is provided in section 2. Section 3 identifies pathways of C_2H_2 formation, presents network diagrams and analyses the hydrocarbon chemistry in a typical T Tauri disk and highlights the differences between using the UMIST (McElroy et al. 2013) and the KIDA (Wakelam et al. 2012)¹ chemical rate databases. The implications of the new chemical network on the mid infrared spectra is described in section 4. Section 5 discusses the results followed by conclusions.

2. Modeling

2.1. Physical disk Modeling

PRODIMO (Version: 2.0-421754a9) is a radiation thermo-chemical code that models the physical and chemical structure of planet forming disks (Woitke et al. 2009, 2016). It assumes an axis-symmetric, Keplerian, irradiated disk. It performs 3D ray based dust continuum radiative transfer to obtain the dust temperature and the wavelength dependent radiation field in the disk (Woitke et al. 2009).

We model a steady-state standard T Tauri star-disk system with a grid point resolution of 150×100 cells. Our disk parameters are the same as in Woitke et al. (2018) except for the radial extent R_{out} . The emitting region of molecules like C_2H_2 in the mid-IR are limited to within 10 au (Woitke et al. 2018). Hence, we cut the radial extent of the disk to 10 au to be able to increase

¹ Note that we use here the published network file kida.uva.2014 from Wakelam et al. (2015), referred to as KIDA2014 in the remainder of this work.

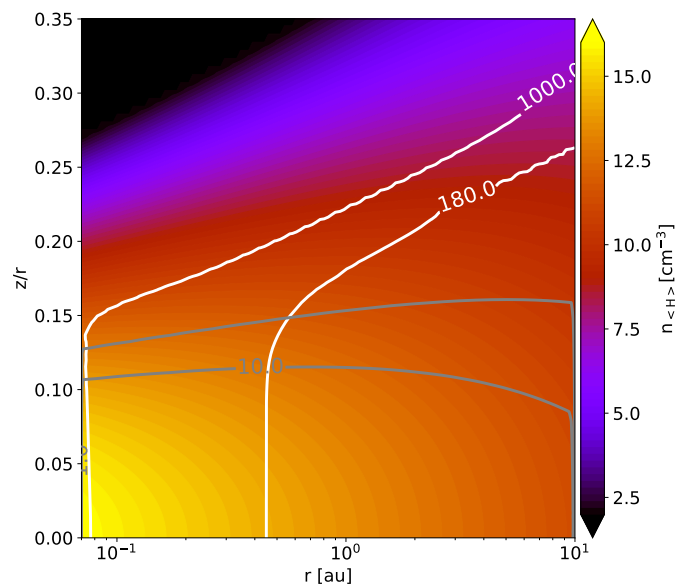


Fig. 1. The particle density ($n_{<H>}$) of the disk in all the subsequent models. The white lines corresponds to the gas temperature of 180 K and 1000 K. The gray contours depict the combined radial and vertical $A_V = 1$ and $A_V = 10$.

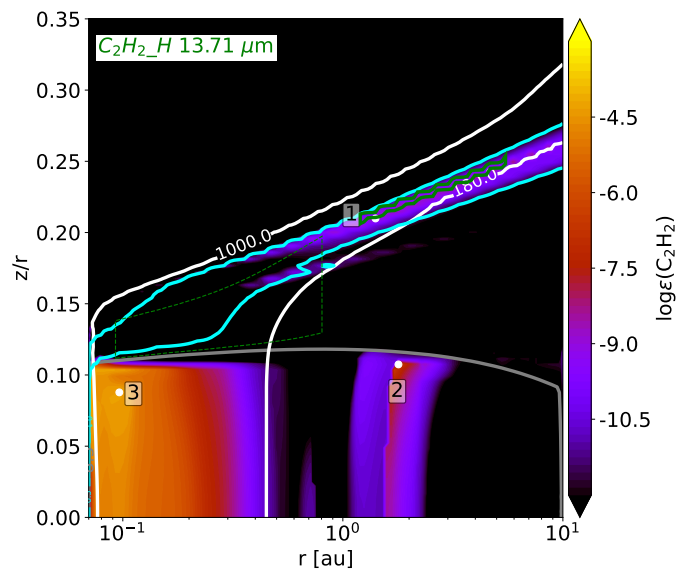


Fig. 2. The abundance of C_2H_2 with respect to $n_{(H)}$ obtained from the fiducial disk model. The white lines show the gas temperature contours for 180 K and 1000 K. The gray contour depicts $A_V = 8.5$. The green dotted line shows the region from which 50% of the continuum emits at $\sim 13.7 \mu m$ (representative of the ν_5 fundamental band). The green solid line shows the region where 50% of the flux is emitted by C_2H_2 at $13.7 \mu m$. The white dots indicate the grid points for which the chemistry is subsequently analysed in detail. The cyan contours depict where 20 and 99% of hydrogen is in the form of H_2 .

the spatial resolution for the inner regions. Our corresponding disk mass M_{disk} inside 10 au is only $9.495 \cdot 10^{-4} M_{\odot}$. We also use the canonical gas-to-dust mass ratio of 100. Figure 1 shows the physical structure of the disk model.

Table 1. The list of all the elements along with their abundances used in all the models.

Elements	12 + log ϵ	Abundance (relative to H)
H	12	1
He	10.98	$9.64 \cdot 10^{-2}$
C	8.14	$1.38 \cdot 10^{-4}$
N	7.90	$7.94 \cdot 10^{-5}$
O	8.48	$3.02 \cdot 10^{-4}$
Ne	7.95	$8.91 \cdot 10^{-5}$
Na	3.36	$2.29 \cdot 10^{-9}$
Mg	4.03	$1.07 \cdot 10^{-8}$
Si	4.24	$1.74 \cdot 10^{-8}$
S	5.27	$1.86 \cdot 10^{-7}$
Ar	6.08	$1.20 \cdot 10^{-6}$
Fe	3.24	$1.74 \cdot 10^{-9}$
PAH	5.48	$3.019 \cdot 10^{-7}$

2.2. Thermo-Chemical disk Modeling

The gas temperature in PRODIMO is determined by the balance between the heating and cooling processes as listed in [Woitke et al. \(2009\)](#). The code uses the kinetic rate approach to obtain the chemical composition in the disk. Additional heating/cooling processes namely the line cooling by molecules emitting in the mid-IR like H₂O, C₂H₂, CH₄, CO₂, NH₃, HCN, OH is included in the model ([Woitke et al. 2018](#)).

The chemical network includes the gas-phase chemistry and gas-grain desorption (thermal desorption, photo-desorption and cosmic-ray desorption) and freeze-out. The chemistry is modeled using 13 elements, namely H, He, C, N, O, Ne, Na, Mg, Si, S, Ar, Fe and PAH. Table 1 lists the elemental abundances used in all the models ([Woitke et al. 2016](#)); we use C/O ratio of 0.457. The fiducial model uses the large DIANA chemical network consisting of 235 species, including atoms, molecules, corresponding positive ions, protonated ions and ices ([Kamp et al. 2017](#)). There are 3037 reactions in the fiducial model that largely originate from the UMIST2012 database ([McElroy et al. 2013](#)). We add two reactions from the KIDA 2014 database, which are explained in Sect. 2.3. The network has a number of specific additional reactions as mentioned in [Kamp et al. \(2017\)](#): X-ray chemistry ([Meijerink et al. 2012](#); [Rab et al. 2018](#)), PAH chemistry (C₅₄H₁₈ is taken as a representative PAH) including adsorption and freeze out (see references in [Kamp et al. 2017](#)), collider reactions from the UMIST 2006 database and photodissociation reactions for the molecular ions ([Heays et al. 2017](#)). Photorates are calculated using the local wavelength dependent radiation field inside the disk ([Kamp et al. 2010](#)). We include a number of three body and thermal decomposition reactions taken from STAND2020 ([Rimmer & Helling 2016](#)) listed in the Appendix A. We take only those reactions from STAND2020 which have valid data for the forward direction²; the backward reactions for the same are not included. H₂ formation is included following [Cazaux & Tielens \(2004\)](#). We explore the impact of using a different H₂ formation rate ([Cazaux & Tielens 2010](#)) in Sect. 4.2.

2.3. Expanding the network for longer hydrocarbon molecules

We aim to analyse the chemical formation and destruction pathways of C₂H₂ and quantify the effect of chemistry on the C₂H₂ abundance and its mid-IR spectra. Our goal is to find potentially missing chemical pathways from the existing chemical network and study their impact on the disk. To do so, we first expand the large DIANA chemical network by adding additional longer hydrocarbon species.

We decided to restrict ourselves to the chemistry up to the most simple cyclic aromatic hydrocarbon, namely C₆H₆. We included species up till eight carbon atoms to take into account the destruction of larger hydrocarbons to form the stable C₆H₆ molecule. The negative ions are omitted except for H⁻. The rule formulated in [Kamp et al. \(2017\)](#) which states to include the ions and protonated forms of the neutral stable closed shell species is followed. We identify the stable species as C₂H₆, C₃H₄, C₃H₆, C₄H₂, C₄H₄, C₄H₆, C₅, C₅H₂, C₅H₄, C₆, C₆H₂, C₆H₆, C₇, C₇H₂, C₇H₄, C₈, C₈H₂. Their ions and protonated forms are added in the network except for C₄H₆. Only the protonated form of this species is added in the network because destruction reactions for C₄H₆⁺ were unavailable in the rate databases.

In a first step, the hydrocarbon species and their isotopomers, if any, for which the destruction and formation reactions are available in the UMIST2012 database are included in the network. The network has the cyclic and linear isotopomers of C₃H denoted as C₃H and CCCH, C₃H₂ denoted as C₃H₂ and H₂CCC, C₃H₃⁺ denoted as C₃H₃⁺ and CH₂CC⁺, respectively. It also has both linear isotopomers of C₃H₄ denoted as CH₂CCH₂ and CH₃CCH.

The reactions for CCCH are taken from KIDA2014. Both the KIDA2014 and the UMIST2012 database do not provide the reactions for the cyclic counterpart c-C₃H⁺ which might be because this species has never been detected in space. The network also misses C₆H₅ and C₆H₄ as neither of the two databases provides the destruction and formation reactions for these species. The KIDA2014 database misses C₃H₆⁺, C₃H₇⁺, C₆H₆⁺, CH₂CCH₂ and UMIST misses CCCH.

This resulted in a total of 92 new hydrocarbon species added to the large chemical DIANA network. Rates for their reactions are taken from either UMIST2012 or KIDA2014. Table 2 summarizes this list and shows the stable species in bold font. Neutral hydrocarbons including the radicals can freeze on the dust grains. The adsorption energies for these neutral species are taken also from the UMIST2012 database. We assumed the same adsorption energies for both the isomers of C₃H₄ due to the lack of individual data. The enthalpy of formation at 0 K is taken from the UMIST and KIDA database, respectively. We were not able to find the heat of formation for C₃H₆⁺, C₄H₄⁺, C₄H₇⁺, C₅H⁺, C₅H₂⁺, C₅H₃⁺, C₅H₄, C₆⁺, C₆H⁺, C₆H₃⁺, C₆H₆⁺, C₆H₇⁺, C₇H⁺, C₇H₂⁺, C₇H₃⁺, C₇H₄⁺, C₇H₅⁺, CH₃C₆H, C₈⁺, C₈H⁺, C₈H₃⁺, C₈H₄⁺, C₈H₅⁺ in the UMIST, the KIDA or the NIST database. Similar to the adsorption energies, we assumed then the enthalpy of formation for isotopomers as equal for these species.

2.4. Chemical Networks

We aim to investigate the changes in the chemistry of C₂H₂ from using different sets of rate coefficients from UMIST2012 and KIDA2014 after expanding the chemical network. We can then analyse the impact of the extended chemical network on the mid-

² A+B+M → C+D+M, reverse of such a reaction is not added

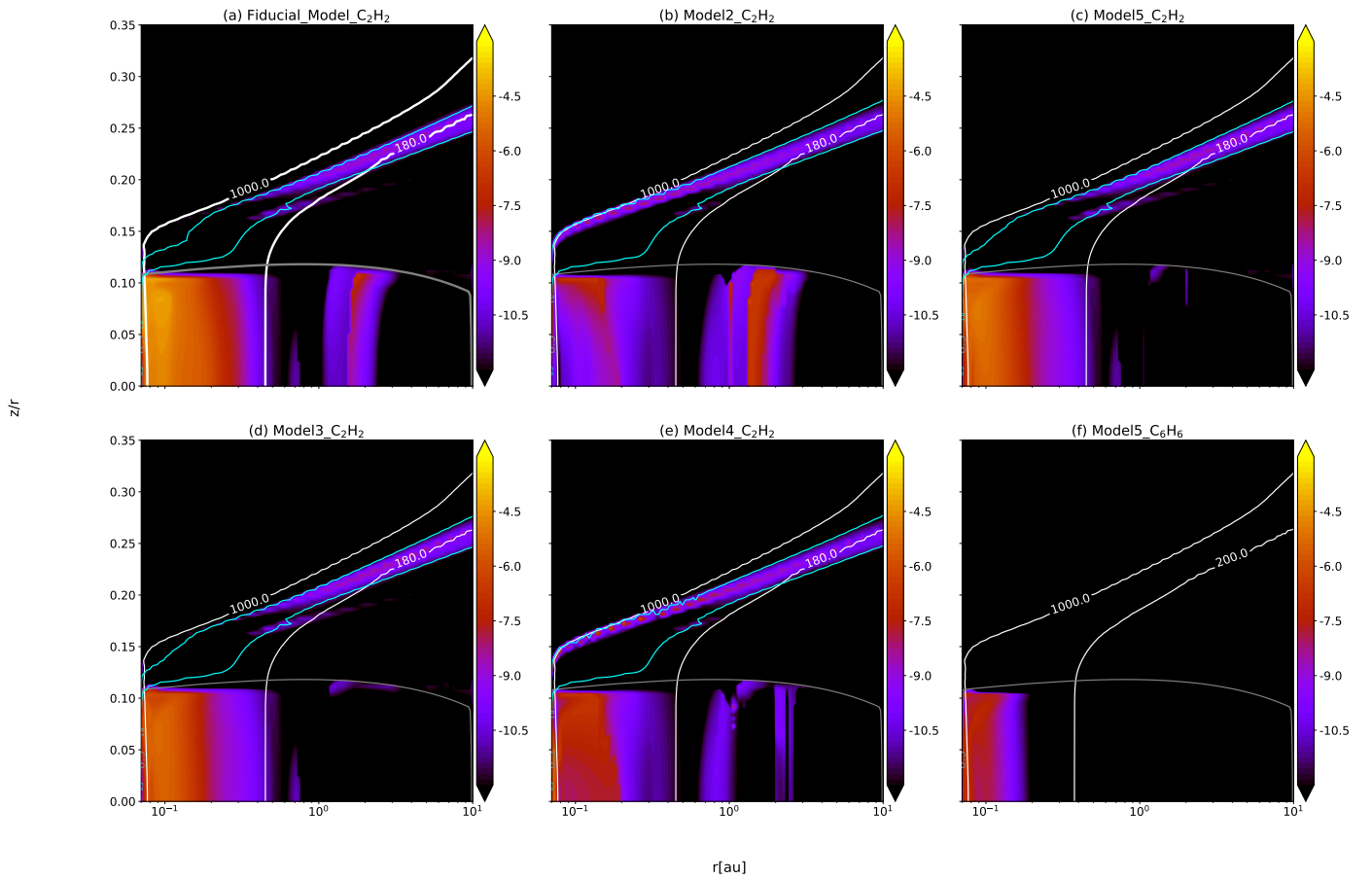


Fig. 3. The abundance of species C_2H_2 , C_6H_6 in different models are shown. The gray contour corresponds to $A_V=8.5$. The temperature contours of 1000 K and 180 K are shown in white. The cyan contours represent where 20 and 99.8% of hydrogen is in the form of H_2 .

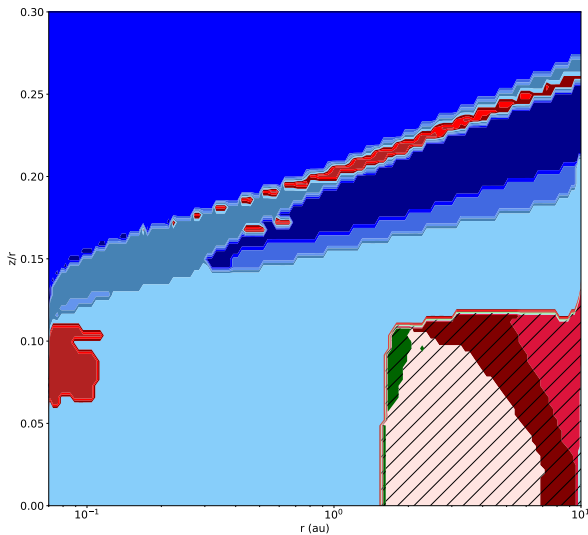


Fig. 4. The distribution of the most abundant hydrocarbons in the fiducial disk model (large DIANA chemistry and UMIST2012 rate coefficients). Each grid point depicts the most abundant hydrocarbon at that location. We do not consider C or C^+ when finding the abundant hydrocarbons.

IR spectra from the disks. To build up our understanding, a series of models was used.

Our fiducial model uses the large DIANA chemical network with 235 species (Kamp et al. 2017), plus the set of three body

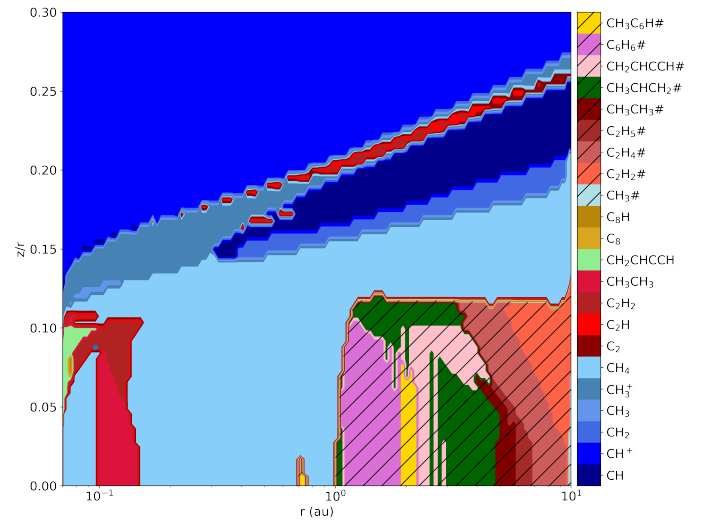


Fig. 5. The distribution of the most abundant hydrocarbons in model 5 (final extended chemical network).

and thermal decomposition reactions listed in Appendix A. The heating and cooling processes that determine the gas temperature are intertwined with the chemistry. Hence, we decided to fix the physical structure of the disk (gas, dust temperatures and densities) to that of the fiducial model for all subsequent models. Only the chemical concentrations were recalculated. This allows

Table 2. The list of all the hydrocarbons present in the extended chemical network.

C	2C	3C	4C	5C	6C	7C	8C
CH	C ₂	C ₃	C ₄	C ₅	C ₆	C ₇	C ₈
CH ₂	C ₂ H	C ₃ ⁺	C ₄ ⁺	C ₅ ⁺	C ₆ ⁺	C ₇ ⁺	C ₈ ⁺
CH ₃	C ₂ H ₂	C ₃ H	C ₄ H ⁺	C ₅ H	C ₆ H	C ₇ H	C ₈ H
CH ₄	C ₂ H ₃	C ₃ H ⁺	C ₄ H	C ₅ H ⁺	C ₆ H ⁺	C ₇ H ⁺	C ₈ H ⁺
CH ⁺	C ₂ H ₄	C ₃ H ₂	HC₄H	C ₅ H ₂	C ₆ H ₂	C ₇ H ₂	C ₈ H ₂
CH ₂ ⁺	C ₂ H ₅	C ₃ H ₂ ⁺	C ₄ H ₃	C ₅ H ₂ ⁺	C ₆ H ₂ ⁺	C ₇ H ₂ ⁺	C ₈ H ₂ ⁺
CH ₃ ⁺	C ₂ ⁺	C ₃ H ₃ ⁺	CH₂CHCCH	C ₅ H ₃ ⁺	C ₆ H ₃ ⁺	C ₇ H ₃ ⁺	C ₈ H ₃ ⁺
CH ₄ ⁺	C ₂ H ⁺	<u>CCCH (l-C₃H)</u>	CH₂CHCHCH₂	CH₃C₄H	C ₆ H ₄ ⁺	C ₇ H ₄ ⁺	C ₈ H ₄ ⁺
CH ₅ ⁺	C ₂ H ₂ ⁺	<u>H₂CCC (l-C₃H₂)</u>	C ₄ H ₂ ⁺	CH ₃ C ₄ H ⁺	C ₆ H ₅ ⁺	C ₇ H ₅ ⁺	C ₈ H ₅ ⁺
CH#	C ₂ H ₃ ⁺	CH ₂ CCH	C ₄ H ₃ ⁺	C ₅ H ₅ ⁺	C₆H₆	CH₃C₆H	C ₈ #
CH ₂ #	C ₂ H ₄ ⁺	CH₃CCH	C ₄ H ₄ ⁺	C ₅ #	C ₆ H ₆ ⁺	C ₇ #	C ₈ H#
CH ₃ #	C ₂ H ₅ ⁺	CH₂CCH₂	C ₄ H ₅ ⁺	C ₅ H#	<u>C₆H₇</u>	C ₇ H#	C ₈ H ₂ #
CH ₄ #	CH₃CH₃	CH₃CHCH₂	C ₄ H ₇ ⁺	C ₅ H ₂ #	C ₆ #	C ₇ H ₂ #	
	CH ₃ CH ₃ ⁺	CH ₂ CCH ⁺	C ₄ #	CH ₃ C ₄ H#	C ₆ H#	CH ₃ C ₆ H#	
	C ₂ H ₇ ⁺	C ₃ H ₄ ⁺	C ₄ H#		C ₆ H ₂ #		
	C ₂ #	C ₃ H ₅ ⁺	HC ₄ H#		C ₆ H ₆ #		
	C ₂ H#	C ₃ H ₆ ⁺	C ₄ H ₃ #				
	C ₂ H ₂ #	<u>C₃H₇⁺</u>	CH ₂ CHCCH#				
	C ₂ H ₃ #	C ₃ #	CH ₂ CHCHCH ₂ #				
	C ₂ H ₄ #	C ₃ H#					
	C ₂ H ₅ #	C ₃ H ₂ #					
	CH ₃ CH ₃ #	<u>CCCH#</u>					
		H ₂ CCC#					
		CH ₂ CCH#					
		CH ₃ CCH#					
		CH ₂ CCH ₂ #					
		<u>CH₃CHCH₂#</u>					

Notes. The species in gray were present in the large DIANA chemical network (and are present in all models). The species in black are added to this network. All these species are present in model 5. All the species except the underlined ones are present in models 3 and 4. The stable species are marked in bold. The ices of neutral species are represented by #.

Table 3. Species missing in the databases. Stable species are marked in bold.

Only in UMIST2012	Only in KIDA2014
C ₃ H ₆ ⁺	CCCH
C ₃ H ₇ ⁺	
C ₆ H ₆ ⁺	
CH₂CCH₂	

to isolate the effect of chemical rates on the species abundances, line emitting regions of the molecules and the mid-IR line fluxes.

Each model has a barrier-less charge exchange and a dissociative recombination formation reaction for C₂H₂ taken from the KIDA2014 database:



³These reactions constitute a dominant formation pathway of C₂H₂ when using KIDA2014 and are therefore added in all the models.

Table 4 summarises the different models that we use in this work. The chemical database and the size of the chemical network are varied in the models. Model 2 uses the large DIANA

³ all the reactions referenced are from within the text

chemical network with the rates calculated using the rate coefficients provided by the KIDA2014 database. Model 3 and model 4 use the new extended chemical network consisting of all the species in Table 2 except the underlined ones and use rate coefficients for reactions primarily taken from UMIST2012 and KIDA2014, respectively. They have the same species to facilitate the comparison between the two databases. This is why they lack seven species, namely C₃H₆⁺, C₃H₇⁺, C₆H₆⁺, CH₂CCH₂(C₃H₄) and its corresponding ice CH₂CCH₂#, and CCCH and its corresponding ice CCCH#⁴. The databases are not complete in providing all the required reactions and species. For example, the UMIST2012 database clubbed c-C₃H₂⁺ and l-C₃H₂⁺ together as C₃H₂⁺ which is used in model 3. We therefore use c-C₃H₂⁺ from the KIDA2014 database as its counterpart in model 4.

Model 5 has the missing seven species included and uses the UMIST2012 database and a few selected reactions added from the KIDA2014 database for CCCH. Model 5 thus presents the complete extended chemical network. Model 5 also includes the following dissociative recombination reaction with electrons



The rate coefficient is taken from the KIDA2014 database.

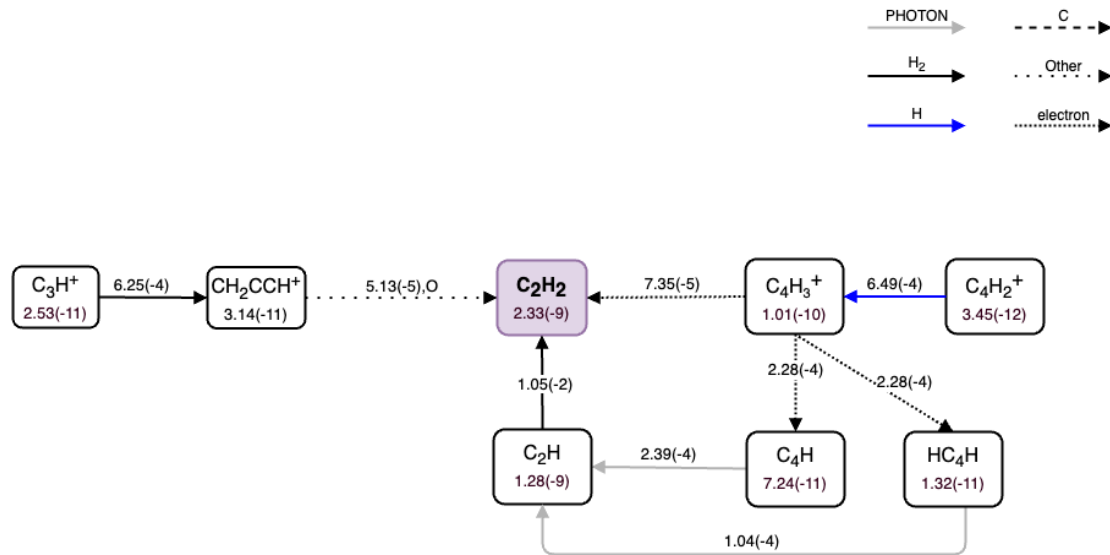


Fig. 7. Zoomed in chemical network showing the formation pathways that become active after adding the longer hydrocarbons. The abundances and rates correspond to model 3 (extended hydrocarbon network using the UMIST2012 rate database). This also highlights the major differences in the formation pathways of C_2H_2 between Fig 6 and 8.

Table 4. List of models used in this paper specifying the details of the chemical network.

Model #	database	# of species	# of reactions
Fiducial	UMIST2012	235	3036
Model 2	KIDA2014	235	3072
Model 3	UMIST2012	320	4004
Model 4	KIDA2014	320	4150
Model 5	UMIST2012	327	4121

in the midplane around 0.1 au and 2 au. This general qualitative structure of the C_2H_2 abundance is the same in all the models no matter which size of network/database we use; only the radial extent changes slightly.

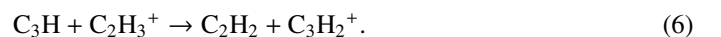
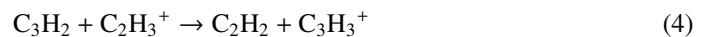
To understand the formation of C_2H_2 in our disk model, we have chosen three representative grid points from the three reservoirs shown as white circles in Fig. 2. Grid point 1 is the representative point for surface chemistry that lies around the emitting region of the C_2H_2 transition at $13.706 \mu\text{m}$ above the continuum emitting surface at $13.7 \mu\text{m}$. This particular transition is chosen as it has the highest flux in the fiducial model. Grid points 2 and 3 reside in regions of maximum abundance of C_2H_2 in the two reservoirs in the midplane. Table 5 summarises the properties of the locations that are analysed. The typical abundance in the models in the surface layers (grid point 1) and the regions beyond $r \leq 1$ au (grid point 3) is of the order of 10^{-9} and 10^{-5} , respectively. The surface layer is confined to a region where the abundance of H_2 is higher than ~ 0.05 , the abundance of H is higher than ~ 0.0019 and the abundance of C is of the order of $\sim 10^{-6}$. The two regions in the midplane are confined by the absence of electrons. In regions with an electron abundance $\geq 10^{-11.5}$, the abundance of C_2H_2 is low ($\leq 10^{-12}$). In the second reservoir around 2 au O is depleted from the gas as it forms H_2O ice. The gas then becomes C-rich and that gives rise to carbon chemistry.

First, the chemistry of C_2H_2 at grid point 1 in the surface layer is analysed. The major formation and destruction pathways of C_2H_2 in the fiducial model are shown in Fig 6. Carbon, being the key ingredient of any hydrocarbon chemistry is unlocked by the photodissociation of CO by UV photons. It can also be un-

locked as C^+ when He^+ dissociates CO. He^+ is produced either by X-rays or cosmic rays depending on which dominates in the surface layers. There are two pathways forming C_2H_2 as shown in the two color-shaded regions of Fig. 6: the neutral-neutral pathway (purple) and the ion-molecule pathway (orange). The formation of C_2H_2 via the neutral-neutral pathway proceeds via the hydrogenation of C. The reaction of H_2 with C forms CH_2 which dissociates to form CH. The reaction of C with H also forms CH. These reactions are barrier less and so depend only on the abundances of H, H_2 and C. Once CH is formed, it can form C_2 via addition of neutral C. This is followed by abstraction of H to form C_2H and finally C_2H_2 . The ion-molecule pathway proceeds through hydrogen addition. Starting from C^+ , this leads to the formation of CH_3^+ via CH^+ . The addition of neutral C then forms $C_2H_3^+$. Again, as these reactions are barrier less, the availability of neutral C is the limiting factor here. Thus for both pathways, the availability of C, H and H_2 is pivotal in deciding the formation route of C_2H_2 in the surface layers. This fundamental chemistry is valid for all the models. The pathways leading to C_2H_2 via C and C^+ are same in all the models. The rates of the reactions differ because of the differences in the abundances and the rate coefficients between the two databases.

C_2H_2 is destroyed to form higher hydrocarbons via the addition of C in the fiducial model. An example is the formation of C_3H . The other destruction path is C_2H_2 photodissociation to C_2H .

In the fiducial model, at grid point 2, we find the ion-molecule chemistry to dominate. The most important pathways forming C_2H_2 are:



These formation pathways are not relevant in the surface layers. As the surface layers are UV dominated, C_3H_2 is photodissoci-

Table 5. Properties of the grid point for which the chemistry was analysed in various models.

point	r,z (au)	T _{gas} [K]	T _{dust} [K]	A _v ^{rad}	A _v ^{ver}	n _{<H>} [cm ⁻³]	χ	remark	reservoirs in fiducial model
1	1.41, 0.30	300	230	1.10	0.021	5.6 · 10 ⁹	3.3 · 10 ⁵	surface layer	H ₂ ,He,O,C,CO
2	1.79, 0.19	85	85	3200	13	1.3 · 10 ¹²	0	outer midplane	H ₂ ,He,CO,C ₃ H ₂ #
3	0.1, 0.0085	480	480	1700	62	2.2 · 10 ¹⁴	0	inner midplane	H ₂ ,He,CH ₄ ,H ₂ O,

Notes. Location describes the radial and vertical direction in the disk model. n_{<H>} is the particle density of H, A_{v,rad} and A_{v,ver} are the radial and vertical visual extinction, χ is the UV radiation field at that location in units of drain field. The final column mentions the main form of C, H, He, O in the reservoir in the surface layers in the fiducial model.

ated to C₃H instead of forming C₂H₂. Figure 3 shows the difference in the abundances for C₂H₂ in all our models which we discuss in the following subsections.

3.1. The extended hydrocarbon chemistry using the UMIST database

In model 3, we add the hydrocarbon species that are common to the UMIST2012 and the KIDA2014 rate database as shown in Table 2. Model 3 only uses reactions from the UMIST2012 rate database. The new C₂H₂ abundances are shown in Fig. 3 (lower left panel). To understand the differences in abundance of C₂H₂ between the fiducial model and this model 3, Fig. 7 highlights the differences in the pathways described in the previous section.

In the surface layers, i.e. grid point 1, the total formation rate of C₂H₂ increases by ~ 41% in model 3 relative to the fiducial model. This increase is due to the new pathways that are active now and which were missing from the fiducial model. Figure 7 shows these new pathways that form C₂H₂.

The other difference is the formation of C₂H via breaking down larger hydrocarbons in model 3. For example, the following two reactions were absent in the fiducial model



C₄H dissociates to smaller hydrocarbon molecules like C₂H and C₂. These two molecules are steps in the formation of C₂H₂ as seen in Fig 6. Enhancing their abundances will propagate and lead to a higher abundance of C₂H₂.

The abundance of C₂H₂ in the outer midplane i.e. grid point 2 drops by 6 orders of magnitude in model 3 with respect to the fiducial model (Fig. 3). Due to the presence of longer hydrocarbons and their corresponding more stable ices, the carbon is bound in the ices of longer hydrocarbons. The most abundant ice at this location is benzene ice C₆H₆#. The gas-phase longer hydrocarbon species are concentrated in the inner midplane regions roughly inside 0.5 au at T_{gas} higher than ~200 K.

In the inner midplane, i.e. grid point 3, the total formation rate of C₂H₂ decreases by an order of magnitude in model 3 compared to the fiducial model resulting in a decrease in abundance by an order of magnitude. The dominant formation pathway in the fiducial model is



This reaction is exactly balanced by the destruction of C₂H₂ via a three body reaction



in model 3 making the thermal decomposition of CH₂CCH by M (where M can be H, He or H₂) the dominant formation pathway. As we go deeper in the disk (r = 0.07au, z = 0.007au, T_{gas} = 1100 K and n_{<H>} = 2.3 · 10¹⁴cm⁻³), we find that these major formation pathways are balanced by neutral-neutral or three body destruction pathways making secondary species like H₂O important in forming C₂H₂.

The neutral-neutral destruction reaction of C₂H₂



is favoured over cosmic ray induced photodissociation of C₂H₂ to form C₂H; this reaction is missing from the fiducial model. This again highlights the importance of adding higher hydrocarbons to determine more reliable C₂H₂ abundances.

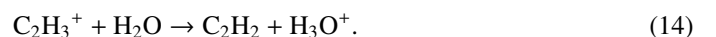
3.2. Role of isomers in the extended hydrocarbon network

We compare models 2 and 4 that is the large DIANA and extended chemical network using the KIDA2014 rate database, respectively. We find two new pathways which are reaction 3 and the dissociative recombination of CH₂CCH⁺ with e⁻ forming C₂H₂ in model 4 (at point 1, Fig B.2). These are the new species added in the extended network. The dissociative recombination reaction of C₃H₂⁺ with e⁻ becomes less important in model 4. This is due to a lowered abundance of C₃H₂⁺. Its formation proceeds through



in model 2. In the extended network, the first step can branch to two isomers, C₃H₃⁺ (c-C₃H₃⁺) and CH₂CCH⁺ (l-C₃H₃⁺) thus lowering the abundance of C₃H₃⁺ consequently lowering the abundance of C₃H₂⁺. However, the decrease in this rate is compensated by the two new pathways above, overall resulting in an increase of ~ 40% in the abundance of C₂H₂ at grid point 1 in model 4.

One of the major formation pathways in both models at grid point 3 is



The thermal decomposition of CH₂CCH by M and dissociative recombination of C₃H₅⁺ with e⁻ add to the production of C₂H₂. Both were missing from the DIANA chemical network thus increasing the C₂H₂ abundance by 2 orders of magnitude in the inner disk midplane region (point 3).

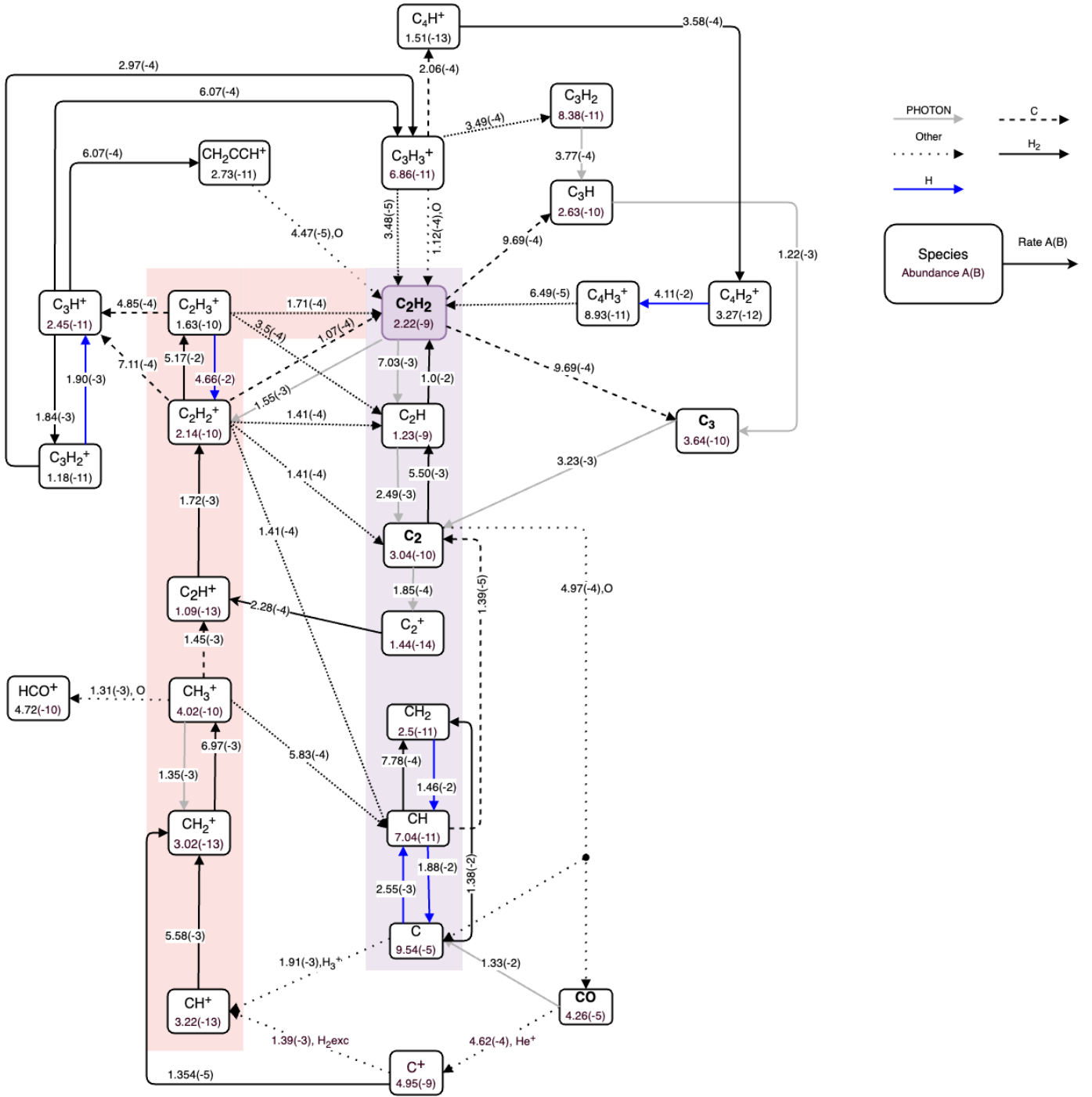


Fig. 8. The chemical network for the surface layers for model 5 (final hydrocarbon network) centered around C_2H_2 .

3.3. Comparison between the UMIST and KIDA rate databases

Figure 3 shows the difference in the radial extent of the surface layer of C_2H_2 in models using the UMIST2012 and the KIDA2014 rate database. We traced this back to the layer with high H_2 abundances extending down to smaller radii in models using the KIDA2014 database. The chemical pathways displayed in Fig. 6 show that H_2 is crucial in the formation of C_2H_2 . Comparing two models using the same chemical network but different rate databases (models 3 and 4), the vertical height at which H/H_2 transition occurs is higher by ~ 0.005 au at the radial distance of 1 au in model 4 (KIDA2014) compared to model 3

(UMIST2012). Models using the UMIST2012 database (fiducial and model 2) have a higher destruction rate of H_2 . There is more destruction of H_2 by atomic oxygen in the UMIST2012 model compared to the KIDA2014 model due to different rate coefficients for the reaction



The C_2H_2 abundance at grid point 3 for model 2 is lower compared to the fiducial model as seen in Fig 3. In the fiducial model, C is locked in C_2H_2 while in model 2 more of the C is in instead CH_4 at the inner midplane (grid point 3). We attribute this difference to missing reactions and different rate coefficients

given in the databases. The reaction



is missing from the KIDA2014 database, but it is one of the dominant destruction reactions for C_2H_3 and the dominant formation reaction for CH_4 and C_2H_2 when using UMIST2012 (fiducial model). The following dominant formation reaction in the fiducial model



has a barrier of 1300 K in KIDA2014 but only 130 K in UMIST2012 explaining the lower rate in model 2. Another important species contributing to the formation of C_2H_2 is C_2H_3^+ . This molecular ion is formed via the reaction



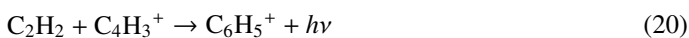
which is a barrierless reaction in UMIST2012 but has an activation energy of 2000 K in KIDA2014. The combination of these differences lead to a lower abundance of C_2H_2 in model 2 at grid point 3 when compared to the fiducial model.

3.4. Benzene formation

Benzene is confined to the inner midplane below $r \leq 0.2$ au and a z/r of ~ 0.1 . It also appears in a narrower radial region in model 4 (KIDA2014, extended hydrocarbon chemistry). To find the dominant formation and destruction pathways in models, we analyse the chemistry in the inner midplane at $r = 0.086$ au and $z/r = 0.07$ with $T_{\text{gas}} = T_{\text{dust}} = 570$ K in an optically thick region with $A_V^{\text{ver}} = 150$ and $A_V^{\text{rad}} = 2400$ and $n_{\text{H}} = 5.6 \cdot 10^{14} \text{cm}^{-3}$. We choose this point as it has the maximum abundance of benzene in model 5 (final extended chemical network). The network might be missing some reaction as the databases are not complete in hydrocarbons with 6 C atoms such as C_6H_4 , C_6H_5 etc. The pathway to form benzene is via CH_4 and C_2H_2 . In model 3 (using UMIST2012), the dominant pathway of formation is



contributing $\sim 90\%$ to the total formation rate followed by



contributing only $\sim 5\%$. C_6H_5^+ reacts further with H_2 to form C_6H_7^+ which subsequently recombines with an electron to form benzene



Model 4 (KIDA2014) also follows the same formation scheme as explained above. However, the abundance of benzene at this location in model 4 is of the order of 10^{-14} but even when analysing the region with the highest abundance (10^{-10}) we find the same formation mechanism which then leads to C_6H_6 via dissociative recombination (reaction 22).

3.5. The final hydrocarbon network

Based on what we learned from the previous comparisons, we compiled the final chemical network that has 327 species in total combining the large DIANA network with 235 species and the 92 additional hydrocarbons from Table 3. The leading database is UMIST2012 as it has more species than KIDA2014 and we add a few reactions picked from the KIDA2014 database as described in Sect. 2.3. The network includes the three body and thermal decomposition reactions as mentioned in Appendix A.

The basic formation and destruction pathways of C_2H_2 remain the same as described in Sect. 3.1. Figure 8 details the chemical pathways in the surface layers of the disk. The dominant reactions forming C_2H_2 are reactions 1,



These were also the dominant formation reactions in model 3 for the surface layers. The addition of new hydrocarbons changes the abundances of C_2H_2 in the inner and outer midplane by 2 and 7 orders of magnitude, respectively, compared to the fiducial model for the reasons explained in previous sections. But it does not affect the C_2H_2 abundances in the surface layers much (increase by a factor of ~ 1.5).

In the final network, the reaction of H_2 with C_6H_5^+ leads to C_6H_7^+ that recombines with an electron to form benzene (see reactions 22 and 21). Reaction 19 contributes $\sim 83\%$ and reaction 20 contributes $\sim 16\%$ to the total formation rate of C_6H_5^+ . Hence, both CH_4 and C_2H_2 contribute to the formation of C_6H_6 with the route through CH_4 being the dominant one. Figures 4 and 5 show the effect of adding complex hydrocarbons and highlights how carbon chain length changes throughout the disk. The shades of blue and red corresponds to the single C and two C atom bearing species. The diversity in the ices also increase on using the extended chemical network. This network will be used for the remainder of the paper.

4. Mid-IR spectra

The extended hydrocarbon chemistry has an effect on the chemical abundances, especially on C_2H_2 . We study here whether this has an impact on the mid-infrared spectra emitted from the disk. We use the escape probability method which yields vertically emitted total line fluxes (Woitke et al. 2009) and FLiTs developed by Michiel Min (Woitke et al. 2018). FLiTs does a full line radiative transfer including the dust continuum and line opacity overlap. We use HITRAN 2009 (Rothman et al. 2009) as our spectroscopic database. The rules for selecting the line transitions are taken from Woitke et al. (2018).

Figure 9 shows the line flux for C_2H_2 calculated using the escape probability method and FLiTs convolved to a resolution of 3000 appropriate for JWST. The weak lines at $\sim 14 \mu\text{m}$ have higher fluxes using the escape probability method compared to FLiTs (see residuals in Fig. 9). The escape probability treatment do not take into account absorption by the continuum which can be an issue for molecules emitting from relatively low heights in the disk. The escape probability produces a factor of 2 higher integrated C_2H_2 ($11.8\text{-}16.22 \mu\text{m}$) flux relative to FLiTs as shown in Fig. 9. In the following, we use FLiTs to calculate the spectra.

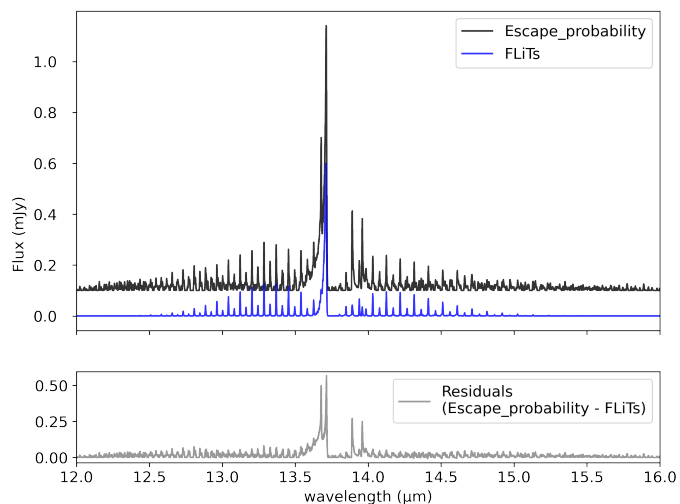


Fig. 9. The flux emitted by C_2H_2 in model 5, convolved at a spectral resolution of $R = 3000$ calculated using the escape probability method (black) and using the FLiTs code (blue). The bottom panel shows the differences in the line flux between the two methods.

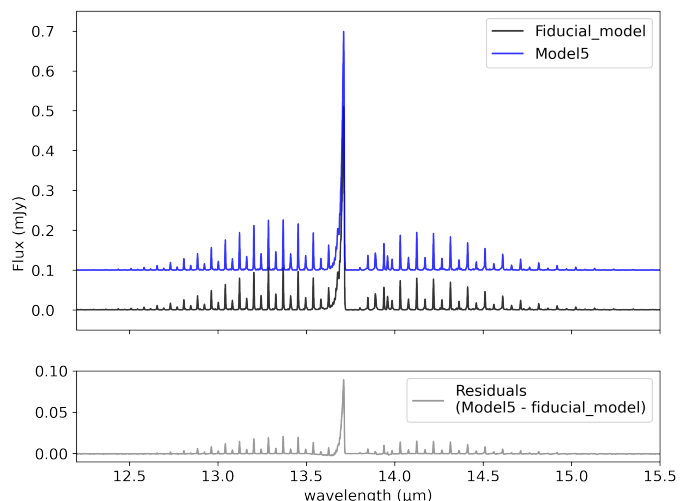


Fig. 10. C_2H_2 flux using the FLiTs code for the model with large DIANA network (fiducial model) and the extended hydrocarbon chemistry (model 5) convolved to the spectral resolution of $R = 3000$. The bottom panel shows the difference in the line flux between the two models.

4.1. Implication on mid-IR spectra

Figure 10 shows the flux emitted by C_2H_2 for the model with the expanded hydrocarbon chemistry (model 5) and the one using the large DIANA chemical network (fiducial model). The total integrated flux in model 5 is higher by 10% relative to the fiducial model. This increase is solely because of the use of the expanded chemical network as we fixed the gas temperature of the disk. The peak fluxes produced in model 5 are ~ 0.6 mJy at $R = 3000$ and ~ 0.33 mJy at $R = 600$. The peak flux for C_2H_2 in T Tauri disks as observed by Spitzer is ~ 20 mJy at a $R = 600$. We find that using an extended chemical network cannot enhance C_2H_2 emission to the typical flux level of mid-infrared observations of T Tauri disks. A wide exploration of disk physical parameters like UV radiation, disk mass etc. using this network is

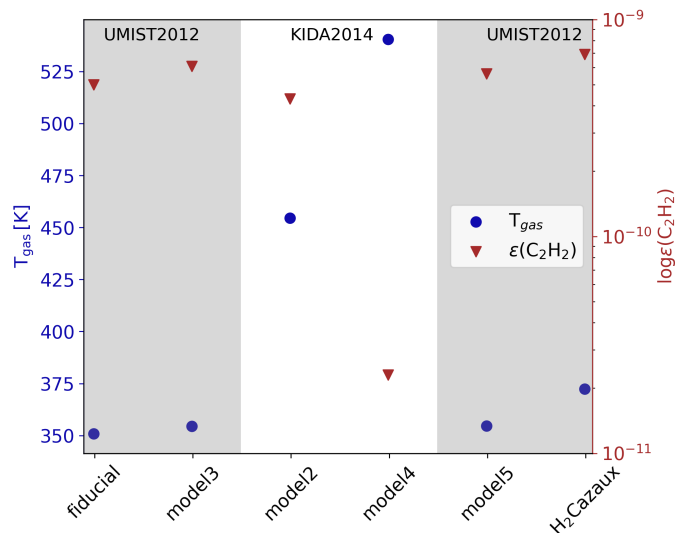


Fig. 11. The gas mass weighted abundance of C_2H_2 (brown) and C_2H_2 abundance weighted gas temperature (blue) of the emitting region of C_2H_2 at $13.71 \mu m$ for all the models. The gray background depicts the models using the UMIST2012 database and white the ones using the KIDA2014 database.

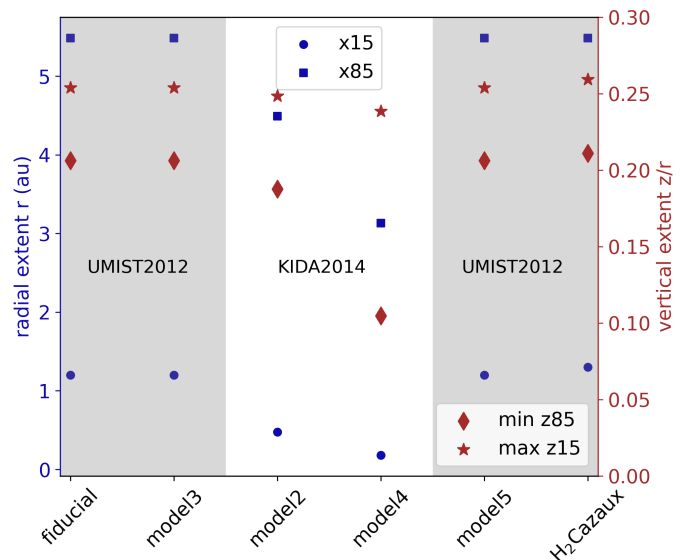


Fig. 12. The effect on the emitting region of the C_2H_2 at $13.71 \mu m$ line due to different chemical networks and the rate databases. The left and right axes depict the maximum radial and vertical extent of the emitting region. $x15$, $x85$, $z15(r)$ and $z85(r)$ denote the radii and heights at which 15 and 85% of the line flux originate, respectively. Min $z85$ and max $z15$ indicate the maximum vertical extent (z/r) of the region. The gray background is used to highlight the models using the UMIST2012 database, while the white background pertains to models using the KIDA2014 database.

now required to identify the key parameters and processes that allow us to reproduce the observed fluxes.

The integrated line flux for C_2H_2 is a factor 3 higher in model 4 (KIDA2014) compared to model 3 (UMIST2012) that have the same chemical network (i.e. equal number of species). The difference arises from the different rate coefficients in the two databases. This leads to the molecular layer being shifted radially inwards in model 4 and being $\sim 50\%$ more vertically extended (see Fig. 12, and also Sect. 3.3). As a result, the

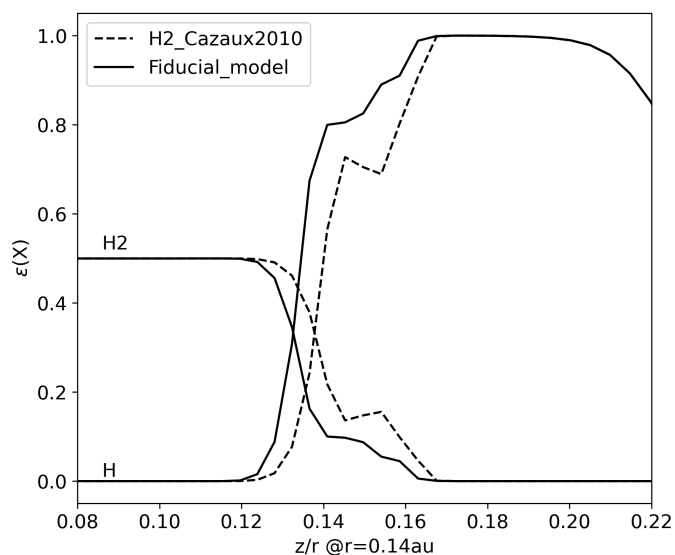


Fig. 13. The effect of using updated H_2 formation rate of Cazaux & Tielens (2010) compared to 2004 on the $H \rightarrow H_2$ transition layer. The figure compares the fiducial model using the large DIANA chemistry with the disk having the extended chemical network using the formation mechanism and the energy barrier reported in Cazaux & Tielens (2010).

C_2H_2 abundance and the abundance weighted gas temperature is higher in model 4 by $\sim 53\%$ (see Fig. 11), which leads to the factor 3 higher line fluxes.

As seen in Fig. 2, in our fiducial model (TTauri disk model, power law surface density profile with a sharp inner edge), only the surface layers contribute towards the mid-IR emission. However, Woitke et al. (submitted) propose a disk model for EX Lupi with a steadily increasing surface density at the inner rim. This fits the spectral energy distribution, the overall shape of the mid-IR spectra observed by JWST, and the observed molecular features and its characteristics like emitting area and gas temperatures. In their model, they find a high abundance of C_2H_2 in the O-rich gas around the inner rim, caused by X-ray irradiation. This region corresponds to our inner midplane (grid point 3) reservoir of C_2H_2 . This recent work shows that for models with a different physical structure, the inner regions (grid point 3) can also contribute to the mid-IR emission.

4.2. The effect of H_2 formation on C_2H_2

In Sect. 3 we show that the H/H_2 transition is important for the abundance of C_2H_2 and in Sect. 4.1 we show that this affects also the flux emitted from this molecule. Hence, the formalism of how H_2 forms may affect the abundance of C_2H_2 in the disk surface layer.

To investigate this, we compare the two approaches of H_2 formation described in Cazaux & Tielens (2004) and Cazaux & Tielens (2010). In cold regions, the formation of H_2 from physisorbed H dominates whereas in warm regions, the formation of H_2 can also proceed via chemisorbed H. Figure 13 shows how the height of the H/H_2 transition (z/r) shifts upwards by 0.005 au at $r = 1$ au when using an improved treatment of mobility of H atoms on grain surfaces at warmer temperatures. Model H_2 Cazaux in Figs. 11 and 12 show the effect on the gas temperature, C_2H_2 abundance and the emitting area of using different databases and the chemical networks. Model H_2 Cazaux used extended chemical network with the UMIST2012 rate database.

The peak flux emitted by C_2H_2 at $\sim 13.7 \mu m$ (Q branch) increases by a factor of ~ 2 (escape probability method) when using the Cazaux & Tielens (2010) formalism. The increase in flux can be attributed to the increased gas temperature of the line emitting region as shown in Fig. 11 when compared to model 5. Also in this case, the surface layer of C_2H_2 extends radially inwards into the inner disk regions as warm temperatures promote the chemisorption channel for H_2 formation.

5. Discussion

We studied various pathways leading to the larger hydrocarbons in protoplanetary disks, specifically C_2H_2 . We isolate the major formation and destruction pathways for C_2H_2 and C_6H_6 and their differences on the basis of whether the UMIST2012 or KIDA2014 rate databases are used. We study the effect of the H/H_2 transition layer on the surface layers of C_2H_2 when using different H_2 formation formalism. We compare in the following the hydrocarbon chemistry from our network in disks to earlier works on hot cores, disks, AGB stars and planetary atmospheres.

5.1. Acetylene

Comparing to previous disk studies, we find that the mechanism to unlock C from CO is the same as described in Bast et al. (2013, and references therein) and Walsh et al. (2015): CO is either photodissociated to C or reacts with He^+ produced by CR or X-ray photons (depending on which one dominates) to form C^+ . The chemistry pathways to form C_2H_2 shown in these studies are similar to what we find. Walsh et al. (2015) do not find the neutral-neutral formation pathway to C_2H from C_2 important. Our chemistry is also similar to that in Agúndez et al. (2008), although their models begin to form CH by C abstracting H from H_2 . This reaction has a high energy barrier (12000 K) and is also reported in Walsh et al. (2015). Despite having this reaction in our disk models, we form CH via radiative association of C and H and destruction of CH_2 which is a barrier-free reaction and has no temperature dependence. This difference arises because Agúndez et al. (2008) follow the time dependent evolution of chemistry with hydrogen being initially molecular.

Warm carbon chain chemistry (WCCC) sources are Class 0/I objects that contain hydrocarbons (e.g. L1527) (Sakai et al. 2008). Densities in WCCCs are of the order of 10^9 cm^{-3} and temperatures are ~ 300 K. The chemistry is initiated by sublimating methane ice, which subsequently reacts with C^+ to form hydrocarbon molecules (Sakai & Yamamoto 2013). The formation of higher hydrocarbons proceeds via addition of C^+ followed by dissociative recombination with e^- or via reaction with CH_4 (Sakai & Yamamoto 2013). The chemistry is completely dominated by ion-neutral chemistry. In our disk models (point 1 which has similar density, temperatures as WCCC sources (see Fig. 1)), we find reactions with C to dominate over reactions with C^+ . Higher hydrocarbons are formed also via addition of neutral C. Addition of H_2 to ions is the main pathway in disks to form higher hydrogenated ion contrary to the addition of CH_4 to molecular ions which occurs in WCCC sources. The high abundances of C^+ required in WCCC sources are maintained either by high cosmic-ray induced ionization (ζ) or high UV. WCCCs can have $\zeta \geq 10^{-16} \text{ s}^{-1}$ (Kalvāns 2021) whereas we use $\zeta = 10^{-17} \text{ s}^{-1}$ in our disk models. We also use a steady state chemistry model while the WCCC models study time dependent chemistry starting from cold icy conditions in dark cores and warming up over short timescales as gravitational collapse

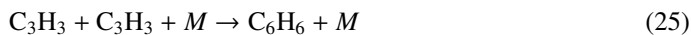
provides energy. So there is also a fundamental difference in timescales of chemistry and history of material.

C-rich Asymptotic giant branch (AGB) stars have been studied in detail by for example [Cherchneff & Glassgold \(1993\)](#); [Millar & Herbst \(1994\)](#). Typical gas temperatures in the inner circumstellar envelopes around AGB stars are ~ 1000 K and densities are the order of 10^{10}cm^{-3} . The neutral-neutral chemistry dominates in these objects while the chemistry in disk surface layers that have similar physical conditions (see Fig. 1) is a mixture of ion-neutral and neutral-neutral chemistry. The difference in the initial abundances between our disk model and that of [Cherchneff et al. \(1993, Table 2\)](#) prevents a direct comparison. The trend of odd-even effect where even numbered C hydrocarbons are more abundant than the odd C (see [Cherchneff & Glassgold 1993, Fig. 3](#)) is also seen in our disk models.

[Loison et al. \(2019\)](#); [Vuitton et al. \(2019\)](#) studied the hydrocarbon chemistry in atmospheres of planets and moons. The chemical networks in these studies take into account the termolecular and pressure dependent reactions. The temperatures range from ~ 80 to 180 K and pressures vary from 10^5 (surface) to 10^{-7} Pascal with altitude ([Hörst 2017](#)). These pressures correspond to a range of $\sim 10^8$ to 10^{20}cm^{-3} of particle densities. The reactions destroying C_2H_2 to form C_2H and C_2 in atmospheres ([Vuitton et al. 2019](#)) are also dominant in the disk surface layers but the physical conditions are not the same, thus preventing an in depth comparison.

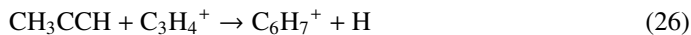
5.2. Benzene

The reactions 20, 21 and 22 forming C_6H_6 are the dominant pathways in both studies ([Loison et al. 2019](#); [Vuitton et al. 2019](#)). We find the same reactions to be the major pathways forming benzene in the disk. The reaction



is found to contribute to form benzene at pressures $\sim 10^{15}$ to 10^{19}cm^{-3} and at temperatures of ~ 160 K in atmospheres ([Loison et al. 2019](#)). However, [Woods & Willacy \(2007\)](#) who include this reaction, did not find it to be important in disks and it is therefore not included in our network.

On comparing the benzene formation routes in models using the UMIST2012 and KIDA2014 database the formation scheme via reactions 20 and 21 leading to C_6H_6 are reported in [McEwan et al. \(1999\)](#) for the interstellar medium and are dominant in both the models. The reaction scheme forming benzene in protostellar environments outlined in [Woods & Willacy \(2007\)](#) as



is not dominant in any of our models. The thermal decomposition reaction of CH_2CCH with M to form C_2H_2 becomes dominant and is favoured over the neutral-neutral reaction of CH_2CCH with H_2 forming CH_3CCH . This decreases the abundance of CH_3CCH resulting in reaction 26 not being dominant.

5.3. Future work

A chemical network can never be complete. Based on the species for which the reactions of formation and destruction were available, the extended network for hydrocarbon chemistry is provided. The difference in rate coefficients from the rate databases affects the chemistry and the abundance of species in the disk, but we show that the impact on the observable C_2H_2 line fluxes is lower than a factor 2.

The values of adsorption energies shift the ice lines and the uncertainties in these thus affect the chemistry. Laboratory measurements of enthalpy of formation for a number of higher hydrocarbon ions are needed as they can also affect the chemical structure of the disk. We also miss species from the chemical network as we are limited by the rate databases. Our network does not include C_6H_5 or C_6H_4 (as explained in Sect. 2.3).

A clear distinction between the isotopomers of species and their rate coefficients needs to be included in the rate databases. KIDA has more species compared to KIDA2014, but it is not in the format of an easy to use ratefile. Often multiple rate coefficients exists and so the user has to decide which rates are better. In addition, the database changes constantly, causing an issue to reproduce results at a later stage. These are fundamental differences to UMIST which clearly recommends rates and has stable releases. Both approaches of course have their pros and cons.

We lack currently the framework to fully take into account the pressure-dependent reactions in PRODIMO which are dominant in planetary atmospheres. Adding these is beyond the scope of this paper and will be the subject of a future study. These reactions might be important in the midplane (point 3) but less so in the surface layers of the disks. It is necessary to test in the future the importance of such reactions for the high density inner disks as we may miss some key pathways.

6. Conclusion

In this paper, we aim to understand the hydrocarbon chemistry in the inner, warm and dense regions of planet-forming disks around T Tauri stars. We present an extended chemical network that includes hydrocarbon species with up to 8 carbon atoms. It includes the linear and cyclic isotopomers of several species, limited by the availability of such data in UMIST2012 and KIDA2014. With this network we can form the simplest cyclic hydrocarbon: Benzene.

We find that a more extended chemistry alone does not explain the high fluxes observed by Spitzer. A more detailed study varying physical parameters of the disk using this chemical network is needed to better interpret the observations. We find that the abundances of C_2H_2 using the extended chemical network increase only by $\sim 40\%$ relative to the large DIANA chemical network in the surface layers (grid point 1). The reservoir of gas-phase C_2H_2 in the outer midplane disappears to form ices of longer hydrocarbons. The abundance in those regions hence drops by 7 orders of magnitude (grid point 2). There is a decreasing gradient of C_2H_2 abundance in the inner midplane which is more prominent in model using the extended chemical network (model 5). With the expanded network, we find that in extremely inner regions of the disk the major C_2H_2 formation pathways were balanced by the neutral-neutral, three body or thermal decomposition destruction pathways making secondary species like H_2O , NH_3 etc important. A detailed analysis of the three-body reactions network is needed and will be the focus of a subsequent paper.

H, H_2 , C and C^+ are crucial to form C_2H_2 . Therefore, the layer at which the H/ H_2 transition occurs is important and thus the details of the H_2 formation mechanism. We find that this transition occurs higher up in the disk when using the updated formalism of H_2 formation ([Cazaux & Tielens 2010](#)). This is also important in determining the radial extent of the surface layer where C_2H_2 is abundant.

The extended chemical network presented here, is important when studying longer hydrocarbons in the disks. With JWST discovering more complex hydrocarbon species in disks more com-

plex chemical modelling is warranted. Our work presents thus a key step forward in modelling the hydrocarbons in disks for future comparison with observations from JWST.

Acknowledgements. This project has received funding from the European Union's Horizon 2020 research and innovation programme under the Marie Skłodowska-Curie grant agreement No. 860470. CHR acknowledges the support of the Deutsche Forschungsgemeinschaft (DFG, German Research Foundation) research Unit "Transition discs" - 325594231. CHR is grateful for support from Max Planck Society. We thank the anonymous referee for their constructive comments.

References

- A. M. Arabhavi, I. K. 2023, *Science*, submitted
- Agúndez, M., Cernicharo, J., & Goicoechea, J. R. 2008, *A&A*, 483, 831
- Anderson, D. E., Blake, G. A., Cleeves, L. I., et al. 2021, *The Astrophysical Journal*, 909, 55
- Bast, J. E., Lahuis, F., van Dishoeck, E. F., & Tielens, A. G. G. M. 2013, *A&A*, 551, A118
- Bergin, E. A., Du, F., Cleeves, L. I., et al. 2016, *ApJ*, 831, 101
- Bethell, T. & Bergin, E. 2009, *Science*, 326, 1675
- Carr, J. S. & Najita, J. R. 2011, *ApJ*, 733, 102
- Cazaux, S. & Tielens, A. G. G. M. 2004, *ApJ*, 604, 222
- Cazaux, S. & Tielens, A. G. G. M. 2010, *ApJ*, 715, 698
- Cherchneff, I. & Glassgold, A. E. 1993, *ApJ*, 419, L41
- Cherchneff, I., Glassgold, A. E., & Mamon, G. A. 1993, *ApJ*, 410, 188
- Draine, B. T. & Bertoldi, F. 1996, *ApJ*, 468, 269
- Duval, S. E., Bosman, A. D., & Bergin, E. A. 2022, *ApJ*, 934, L25
- Greenwood, A. J., Kamp, I., Waters, L. B. F. M., Woitke, P., & Thi, W. F. 2019a, *Astronomy and Astrophysics*, 626, A6
- Greenwood, A. J., Kamp, I., Waters, L. B. F. M., Woitke, P., & Thi, W. F. 2019b, *Astronomy and Astrophysics*, 631, A81
- Guzmán, V. V., Bergner, J. B., Law, C. J., et al. 2021, *ApJS*, 257, 6
- Heays, A. N., Bosman, A. D., & van Dishoeck, E. F. 2017, *A&A*, 602, A105
- Henning, T. & Semenov, D. 2013, *Chemical Reviews*, 113, 9016
- Hörst, S. M. 2017, *Journal of Geophysical Research: Planets*, 122, 432
- Ilee, J. D., Walsh, C., Booth, A. S., et al. 2021, *ApJS*, 257, 9
- Kalváns, J. 2021, *ApJ*, 910, 54
- Kamp, I., Thi, W. F., Woitke, P., et al. 2017, *Astronomy and Astrophysics*, 607, A41
- Kamp, I., Tilling, I., Woitke, P., Thi, W. F., & Hogerheijde, M. 2010, *A&A*, 510, A18
- Kress, M. E., Tielens, A. G. G. M., & Frenklach, M. 2010, *Advances in Space Research*, 46, 44
- Loison, J. C., Dobrijevic, M., & Hickson, K. M. 2019, *Icarus*, 329, 55
- McElroy, D., Walsh, C., Markwick, A. J., et al. 2013, *A&A*, 550, A36
- McEwan, M. J., Scott, G. B. I., Adams, N. G., et al. 1999, *ApJ*, 513, 287
- Meijerink, R., Aresu, G., Kamp, I., et al. 2012, *A&A*, 547, A68
- Millar, T. J. & Herbst, E. 1994, *A&A*, 288, 561
- Pontoppidan, K. M., Salyk, C., Blake, G. A., et al. 2010, *ApJ*, 720, 887
- Qi, C., Öberg, K. I., Wilner, D. J., & Rosenfeld, K. A. 2013, *ApJ*, 765, L14
- Rab, C., Güdel, M., Woitke, P., et al. 2018, *A&A*, 609, A91
- Rimmer, P. B. & Helling, C. 2016, *The Astrophysical Journal Supplement Series*, 224, 9
- Rothman, L. S., Gordon, I. E., Barbe, A., et al. 2009, *J. Quant. Spectr. Rad. Transf.*, 110, 533
- Sakai, N., Sakai, T., Hirota, T., & Yamamoto, S. 2008, *ApJ*, 672, 371
- Sakai, N. & Yamamoto, S. 2013, *Chemical Reviews*, 113, 8981
- Salyk, C., Pontoppidan, K. M., Blake, G. A., et al. 2008, *ApJ*, 676, L49
- Santoro, G., Martínez, L., Lauwaet, K., et al. 2020, *The Astrophysical Journal*, 895, 97
- Tabone, B., Bettoni, G., van Dishoeck, E. F., et al. 2023, *Nature Astronomy* [arXiv:2304.05954]
- Vuitton, V., Yelle, R. V., Klippenstein, S. J., Hörst, S. M., & Lavvas, P. 2019, *Icarus*, 324, 120
- Wakelam, V., Herbst, E., Loison, J. C., et al. 2012, *ApJS*, 199, 21
- Wakelam, V., Loison, J. C., Herbst, E., et al. 2015, *ApJS*, 217, 20
- Walsh, C., Nomura, H., & van Dishoeck, E. 2015, *A&A*, 582, A88
- Woitke, P., Kamp, I., & Thi, W. F. 2009, *Astronomy and Astrophysics*, 501, 383
- Woitke, P., Min, M., Pinte, C., et al. 2016, *Astronomy and Astrophysics*, 586, A103
- Woitke, P., Min, M., Thi, W. F., et al. 2018, *A&A*, 618, A57
- Woods, P. M. & Willacy, K. 2007, *The Astrophysical Journal*, 655, L49

Table A.1. The list of three body and thermal decomposition reactions added.

Reactions	α	β	γ
CH + M → C + H + M	3.16E-10	0.00E+00	3.37E+04
CN + M → C + N + M	1.09E-9	0.00E+00	7.10E+04
H + H + M → H ₂ + M	9.13E-33	-6.00E-01	0.00E+00
H + N + M → NH + M	5.02E-32	0.00E+00	0.00E+00
N + N + M → N ₂ + M	1.25E-32	0.00E+00	0.00E+00
N + O + M → NO + M	3.26E-33	0.00E+00	0.00E+00
C ₂ H + M → C ₂ + H + M	5.00E-01	-5.16E+00	5.74E+04
C ₂ O + M → C ₂ + O + M	5.00E-01	-5.16E+00	5.74E+04
CH ₂ + M → CH + H + M	9.33E+00	0.00E+00	4.51E+04
HCN + M → HNC + M	1.45E-06	1.00E+00	2.38E+04
CN + H + M → HCN + M	9.35E-30	-2.00E+00	5.20E+20
CO + O + M → CO ₂ + M	1.20E-32	0.00E+00	2.16E+03
NH ₂ + M → NH + H + M	1.99E-09	0.00E+00	3.83E+04
H + CH ₂ + M → CH ₃ + M	5.63E-31	0.00E+00	0.00E+00
NH ₃ + M → NH + H ₂ + M	1.05E-09	0.00E+00	4.70E+04
OCN + M → CO + N + M	3.95E-06	-1.90E+00	3.01E+04
H + C ₂ H + M → C ₂ H ₂ + M	2.63E-26	-3.10E+00	7.21E+02
H ₂ CO + M → CO + H ₂ + M	9.40E-09	0.00E+00	3.32E+04
C ₂ H ₂ + M + H → M + C ₂ H ₃ + M	4.87E-30	-1.07E+00	8.38E+01
H + C ₂ H ₄ + M → C ₂ H ₅ + M	9.23E-29	-1.51E+00	7.29E+01
H + C ₂ H ₅ + M → CH ₃ CH ₃ + M	2.00E-28	-1.50E+00	0.00E+00
H + C ₂ H ₃ + M → C ₂ H ₄ + M	1.49E-29	-1.00E+00	0.00E+00
CH ₂ OH + M + H → CH ₃ OH + M	1.20E-29	1.04E+00	0.00E+00
CH ₃ O + H + M → CH ₃ OH + M	7.21E-30	1.24E+00	0.00E+00
H ₂ CO + H + M → CH ₃ O + M	1.80E-31	6.60E-01	8.63E+02
CH ₂ OH + M → H ₂ CO + H + M	1.66E-10	0.00E+00	1.26E+04
C ₂ H + M → C ₂ + H + M	5.00E-01	-5.16E+00	5.74E+04
C ₂ O + M → C ₂ + O + M	5.00E-01	-5.16E+00	5.74E+04
H + C ₂ H ₃ + M → C ₂ H ₄ + M	1.49E-29	-1.00E+00	0.00E+00
C ₂ H ₄ + M → C ₂ H ₂ + H ₂ + M	5.80E-08	0.00E+00	3.60E+00
H + C ₄ H + M → HC ₄ H + M	2.64E-26	-3.10E+00	7.21E+02
C ₂ H + C ₂ H + M → HC ₄ H + M	5.56E-28	-3.00E+00	3.00E+02
H + C ₄ H ₃ + M → CH ₂ CHCCH + M	5.41E-23	-3.97E+00	1.77E+02
H + HC ₄ H + M → C ₄ H ₃ + M	3.53E-25	-2.93E+00	1.76E+02
C ₂ H ₂ + C ₂ H ₂ + M → CH ₂ CHCCH + M	3.78E-31	1.00E+00	1.86E+00
CH ₃ CH ₃ + M → C ₂ H ₄ + H ₂ + M	3.80E-07	0.00E+00	3.40E+04
CH ₂ CCH + M → C ₂ H ₂ + CH + M	1.00E-14	0.00E+00	0.00E+00
C ₄ H ₃ + M → C ₂ H ₂ + C ₂ H + M	5.34E-05	1.00E+00	4.15E+04
H + e ⁻ + M → H ⁻ + M	2.50E-31	-1.50E+00	0.00E+00
HS + H + M → H ₂ S + M	1.00E-30	-2.00E+00	0.00E+00
H ₂ + S + M → H ₂ S + M	1.40E-31	-1.90E+00	8.14E+03
CO + S + M → OCS + M	3.00E-33	0.00E+00	1.00E+03
CH ₃ ⁺ + H ₂ + M → CH ₅ ⁺ + M	1.10E-28	0.00E+00	0.00E+00
C ₂ H ₂ ⁺ + C ₂ H ₂ + M → C ₄ H ₄ ⁺ + M	1.60E-26	0.00E+00	0.00E+00
C ₂ H ₂ ⁺ + H ₂ + M → C ₂ H ₄ ⁺ + M	1.20E-27	0.00E+00	0.00E+00
C ₂ H ₃ ⁺ + H ₂ + M → C ₂ H ₅ ⁺ + M	1.49E-29	0.00E+00	0.00E+00

Appendix A: Reactions taken from STAND2020

We list the three body and thermal decomposition reactions that are taken from STAND2020 network and are included in our models. As three body reactions are pressure dependent, we take the low pressure rate coefficients for these reactions. A detailed analysis to formulate a complete three body reaction network will be left for future work.

Appendix B: C₂H₂ formation/destruction pathways in KIDA2014

The following figures show the major formation and destruction pathways leading to C₂H₂ when using the KIDA2014 database in model 2 (using large DIANA network) and model 4 (using extended hydrocarbon network).

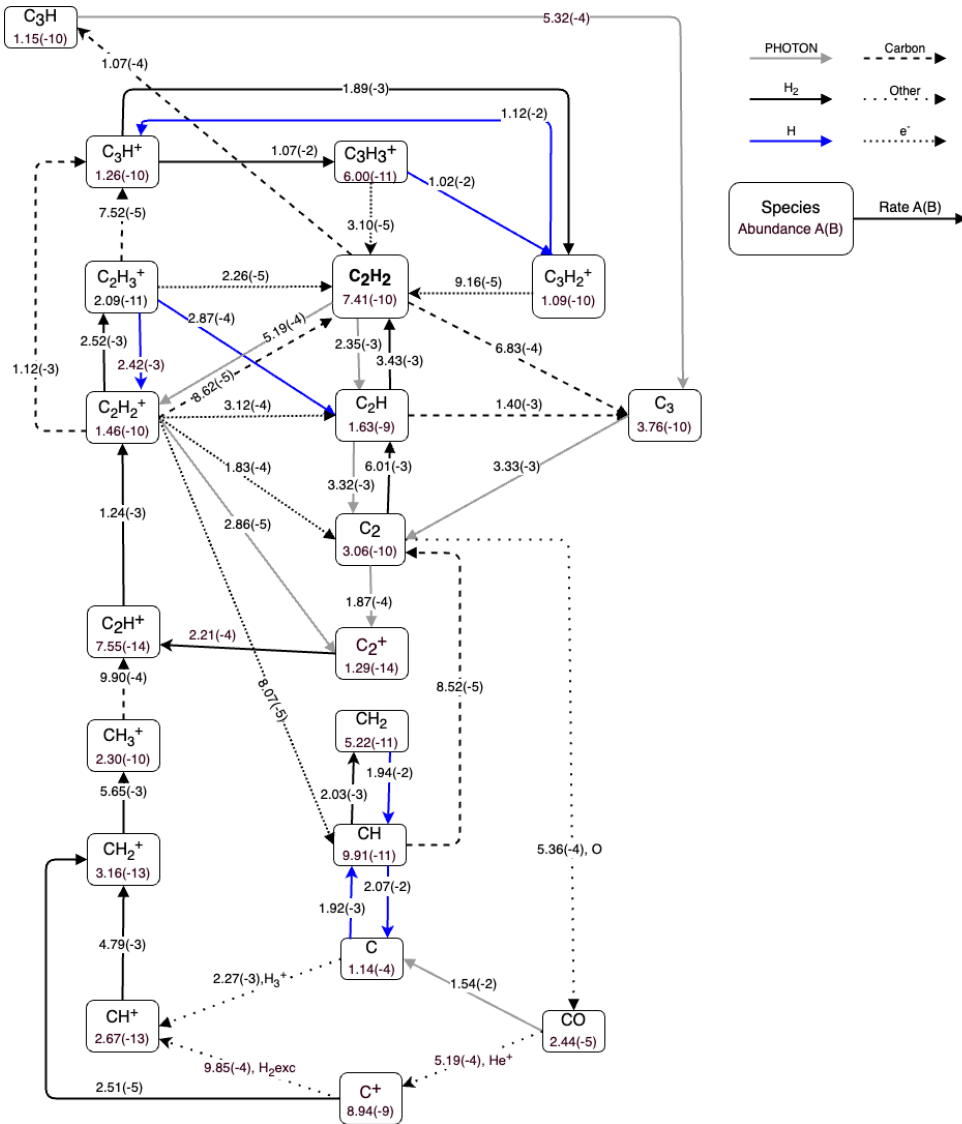


Fig. B.1. The chemical network centered around C_2H_2 depicting the dominant formation and destruction pathways of parent molecules for model 2 (large DIANA network using the KIDA2014 rate database).

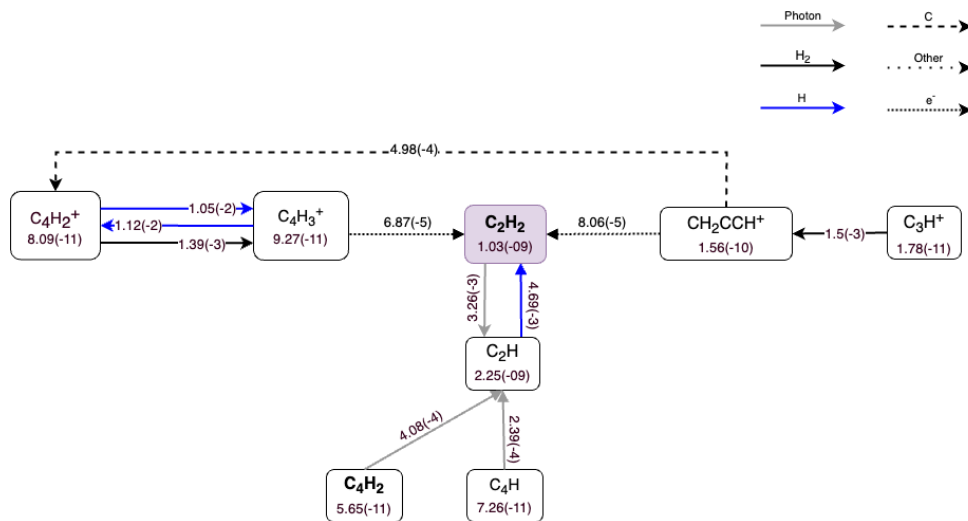


Fig. B.2. Zoomed in chemical network for the extended hydrocarbon chemistry in model 4 (KIDA2014) showing the new pathways forming C_2H_2 and C_2H that were not dominant in model 2 (UMIST2012). Shown are only two steps in the formation pathway.